Multistage work hardening assisted by multi-type twinning in ultrafine-grained heterostructural eutectic high-entropy alloys

Peijian Shi [1], Yunbo Zhong [1,*], Yi Li [1], Weili Ren [1], Tianxiang Zheng [1], Zhe Shen [1], Bing Yang [1], Jianchao Peng [2], Pengfei Hu [2], Yong Zhang [3], Peter K. Liaw [4,*], Yuntian Zhu [5,6,*]

[1] State Key Laboratory of Advanced Special Steel & Shanghai Key Laboratory of Advanced Ferrometallurgy & School of Materials Science and Engineering, Shanghai University, Shanghai 200072, China
[2] Laboratory for Microstructures, Shanghai University, Shanghai 200444, China
[3] State Key Laboratory for Advanced Metals and Materials, University of Science and Technology Beijing, Beijing 100083, China
[4] Department of Materials Science and Engineering, The University of Tennessee, Knoxville, TN 37996, USA
[5] Nano and Heterogeneous Materials Center, School of Materials Science and Engineering, Nanjing University of Science and Technology, Nanjing 210094, China
[6] Department of Materials Science and Engineering, North Carolina State University, Raleigh, NC 27695, USA

High strength of materials usually comes with low ductility due to the lost or short-lived strain hardening. Here, we uncover a sequentially-activated multistage strain hardening (SMSH) that allows for sustained and effective strain-hardening capability in strong ultrafine-grained eutectic high-entropy alloy (EHEA). Consequently, exceptional ductility is realized in an ultrafine-grained EHEA, accompanied with high ultimate strength. We demonstrate that the SMSH is derived from a coordinated three-level design on structural heterogeneity, grain-size control, and intragranular composition modification, which enables the sequential activation of stress-dependent multiple hardening mechanisms. Furthermore, despite the well-known low twinning propensity due to ultrafine grains and medium-to-high stacking fault energies of prototype EHEAs, our coordinated design sequentially activates three types of deformation twinning to assist this SMSH. This work sheds light on the SMSH effect assisted by multi-type twinning previously unexpected in ultrafine-grained EHEAs, and thereby represents a promising route for improving ductility of high-strength materials.

Introduction

Pursuit for materials with high strength and ductility has been a lasting endeavor for the materials community for scientific interests, critical applications, and energy conservation [1–15]. Refining grains to the nano/ultrafine-grained regime can make metals and alloys several times stronger, but this usually comes at a dramatic loss of ductility [2–6,15]. This is because such strengthening often comes at the expense of strain hardening, since upon straining the conventional intragranular dislocation storage, a major mechanism for strain hardening, dramatically disappears in ultrafine-grained (UFG) materials [3,6,15]. To date intensive efforts have been devoted to exploring various other strain-hardening mechanisms, such as deformation twinning (DT), for improving the ductility of UFG materials [3,15,16]. But the DT typically requires materials to have low stacking-fault energies (SFEs) under routine deformation conditions [15–20]. Moreover, this SFE-dependent hardening mechanism is mostly short lived in ultrafine grains due to the high activation stress generally required for DT [15–17,21,22]. As expected, the DT becomes difficult in UFG materials when the grain size is out of the opti-

* Corresponding authors.
E-mail addresses: Zhong, Y. (yunboz@staff.shu.edu.cn), Liaw, P.K. (pliaw@utk.edu), Zhu, Y. (ytzhu@ncsu.edu).

https://doi.org/10.1016/j.mattod.2020.09.029

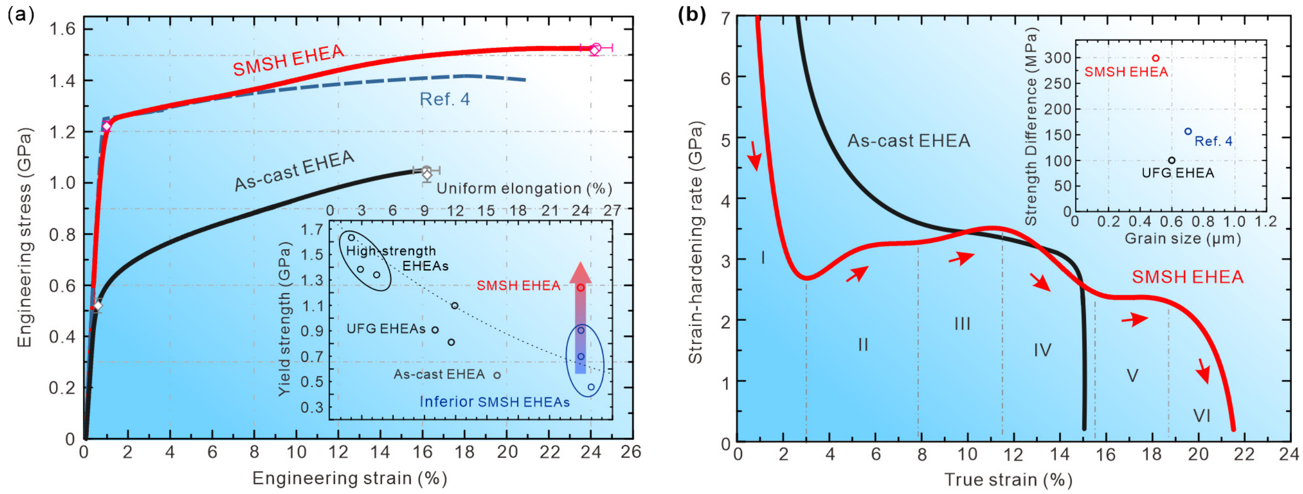

FIGURE 1

Mechanical behaviors. (a) Tensile curves of the as-cast EHEA and the SMSH EHEA. The inset shows the map of yield strength and uniform elongation, including these reported UFG EHEAs [37–39] and high-strength EHEAs [40,41]. Typically, EHEAs with high strength exhibit disappointingly low uniform elongation. Compared to other inferior SMSH EHEAs (Supplementary Fig. 11a), our SMSH EHEA achieves the highest strength without compromising the elongation. The error bars are standard deviations of the mean. (b) The corresponding strain-hardening response. Intriguingly, our EHEA comprises six strain-hardening stages (i.e., Seg. I–VI), which is extremely rare in ultrafine-grained materials. The inset highlights that under comparable $\sigma_{0.2}$, our SMSH EHEA with the smallest average grain size shows a maximum difference between σ_{US} and $\sigma_{0.2}$, indicating the robust strain-hardening ability.

mum range for twinning [16,17], and strain hardening remains inadequate to sustain high uniform tensile ductility after yielding at high stresses. Therefore, in some low-SFE metallic materials, although grain refinement to ultrafine ranges (<500 nm) improves their strength, for example, 1-GPa or higher yield strength obtained in high-entropy alloys [23,24] and high-strength steels [25,26], it often severely sacrifices ductility.

Our recent studies [4] revealed that deploying a heterogeneous dual-phase lamella structure in the UFG eutectic high-entropy alloy (EHEA) [27–31] was able to produce high strength and good ductility. Specifically, this heterostructure was particularly effective in generating the hetero-deformation induced hardening, thus enabling excellent uniform tensile elongation of ~18% at ultrahigh yield strength (~1.25 GPa) [4,12]. Unfortunately, the difference between ultimate and yield strengths was very low (~150 MPa) in our EHEA, as consistently observed in many reported well-optimized UFG materials [32–35]. The low strength difference renders materials poor deformation resistance after yielding, and limits their capability to resist accidental overloading during service. In severe cases, this overloading may lead to catastrophic fracture of materials, which consequently creates enormous risks for engineering structures as well as for human lives. In general, this low strength difference reflects still insufficient strain hardening of materials, which has limited ability to help obtain high ultimate strength and large strength difference, despite improving the uniform elongation [8,12,15]. Therefore, it is of great significance to achieve high enough strain hardening in UFG materials for high uniform elongation, and large difference between ultimate and yield strengths.

Here we report a strong strain-hardening strategy of sequentially-activated multistage strain hardening (SMSH) in UFG materials. Hence the corresponding UFG materials are also referred as the SMSH materials in this work. As-cast $Fe_{20}Co_{20}Ni_{41}Al_{19}$ EHEAs [36] with medium-to-high SFEs (Supplementary Figs. 1, 2) were selected as the prototype alloy to investigate the SMSH behavior. By employing simple cold-rolling and annealing treatments, we engineered a series of EHEAs with the SMSH behavior (see *Materials and methods*). Here, we only focused on an optimal SMSH EHEA with ultrafine grain size of ~500 nm. We demonstrated that this SMSH behavior in our UFG EHEA was stemmed from a coordinated three-level design on hierarchical heterostructure, grain-size control, and intragranular composition modification. This consequently not only improved the ability of dislocation storage, especially maximizing the storage of geometrically necessary dislocations, but also activated extensive deformation twins to assist the SMSH behavior in our UFG EHEA. Unexpectedly, in these activated twins we identified three distinct types of twinning mechanisms, which differ from the classical pole mechanism [16] for twinning that has been widely observed in low-SFE high-entropy alloys (HEAs) in recent years [18–20]. These multiple hardening mechanisms were sequentially activated to sustain lasting and effective strain hardening, which resulted in exceptional uniform elongation, together with high ultimate-yield strength difference, in our high-strength UFG EHEAs.

Results

Tensile behaviors

Remarkable strength–ductility combination and sequential multistage strain-hardening behavior were achieved in our UFG EHEA (Fig. 1). As shown in Fig. 1a, the yield strength ($\sigma_{0.2}$) of our UFG EHEA reached 1.22 ± 0.02 GPa, which was more than twice that of the as-cast EHEA (0.52 ± 0.03 GPa). Nevertheless, this trend did not sacrifice ductility. Instead, the uniform elongation (ε_u), which is a measure of ductility, became better, increasing from 16.17 ± 1.04% for the as-cast EHEA to 24.24 ± 1.26% for our UFG EHEA, accompanied with high ultimate strength (σ_{US})

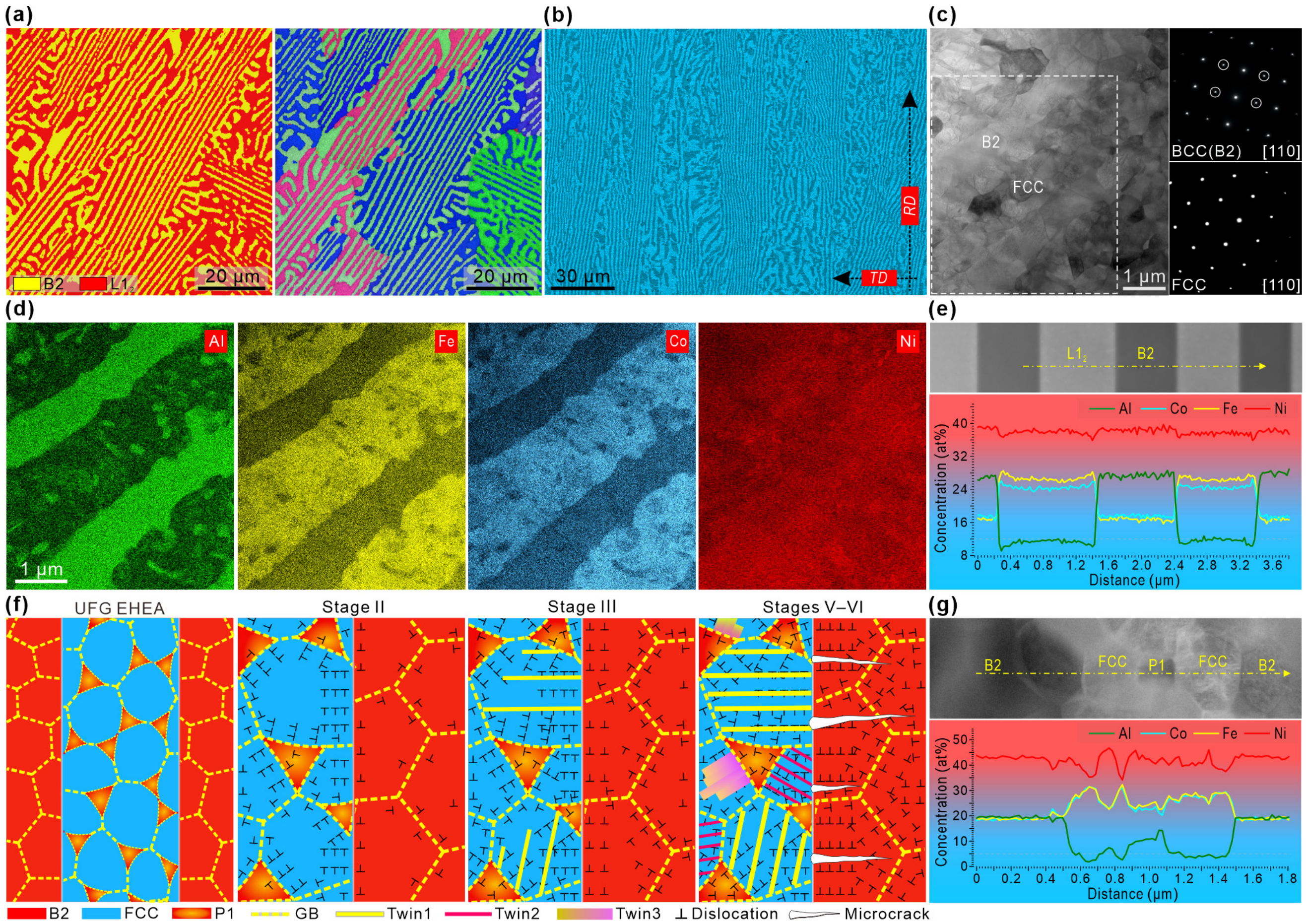

FIGURE 2

Microscopic structure. (a) Electron back-scattering diffraction phase and inverse-pole-figure maps of the as-cast EHEA. (b) Scanning-electron-microscope image of the SMSH EHEA. RD, rolling direction; TD, transverse direction. (c) Transmission-electron-microscopy (TEM) image of the SMSH EHEA, and related selected-area-diffraction patterns (SADPs) of B2 and FCC lamellae. Superlattice-diffraction spots are indicated by white circles. (d) Energy-dispersive-spectroscopy (EDS) maps of the identical region marked in (c) showing the distribution of Al, Fe, Co, and Ni. (e) High-angle annular dark-field scanning TEM (HAADF-STEM) image of the as-cast EHEA, and related EDS composition profiles. (f) A schematic showing different deformation stages in our SMSH EHEA. GB, grain boundary. Twin1-3, three types of twinning. (g) HAADF-STEM image of the SMSH EHEA, and related EDS composition profiles. Labeling all intergranular B2 precipitates as P1.

of 1.52 ± 0.02 GPa. Under comparable $\sigma_{0.2}$, the nominal ε_u of our EHEA is ~2–5 times of those reported for UFG EHEAs [37–39] and high-strength EHEAs [40,41] (Fig. 1a, inset). But it should be cautioned to compare the ductility in the inset of Fig. 1a, because in those reported UFG and high-strength EHEAs [38–41] the gauge length of their dog-bone tensile specimens is as small as 2 mm, and the gauge length-to-width ratio is ~2. Such miniature specimens may cause an overestimation for tensile properties (Supplementary Fig. 3), especially the ductility [42–44]. Zhao et al. showed that work hardening and ductility in Cu significantly increased with decreasing gauge length, and for instance, the measured ε_u of tensile specimens with 2-mm gauge length was twice that of specimens with normal gauge of 10 mm [43,44]. Hence, some excellent UFG EHEAs reported recently are not selected in this comparison (inset, Fig. 1a) due to their small sample dimensions [40,41,45,46].

No doubt that the high ε_u could be attributed to the tailored SMSH behavior in our UFG EHEA (Fig. 1b). The SMSH behavior makes it possible for high strain hardening to last longer [47], which is imperative for maintaining ε_u to high applied strains. Furthermore, this SMSH behavior enabled the ultimate-yield strength difference as high as 300 MPa (i.e., $\sigma_{US} - \sigma_{0.2} = 300$ MPa), which was extremely challenging under such harsh conditions of high $\sigma_{0.2}$ as well as ultrafine grains [4,6,8]. When compared with our recently-reported work [4], the strong SMSH not only further increased the ε_u from ~18% to 24%, but more importantly, doubled the strength difference, at the same level of $\sigma_{0.2}$ (Fig. 1b, inset). Overall, these mechanical properties provide for good safety margin against fracture, which is vital for reliability in engineering structures. Furthermore, it indicates that we can significantly ductilize high-strength UFG materials and obtain high difference between σ_{US} and $\sigma_{0.2}$ using this prominent SMSH behavior.

Microstructure characterization

To clarify the underlying mechanisms of the SMSH behavior, we conducted microstructural investigations, which reveal: (i) Similar to the as-cast EHEA, our UFG EHEA also has alternating dual-

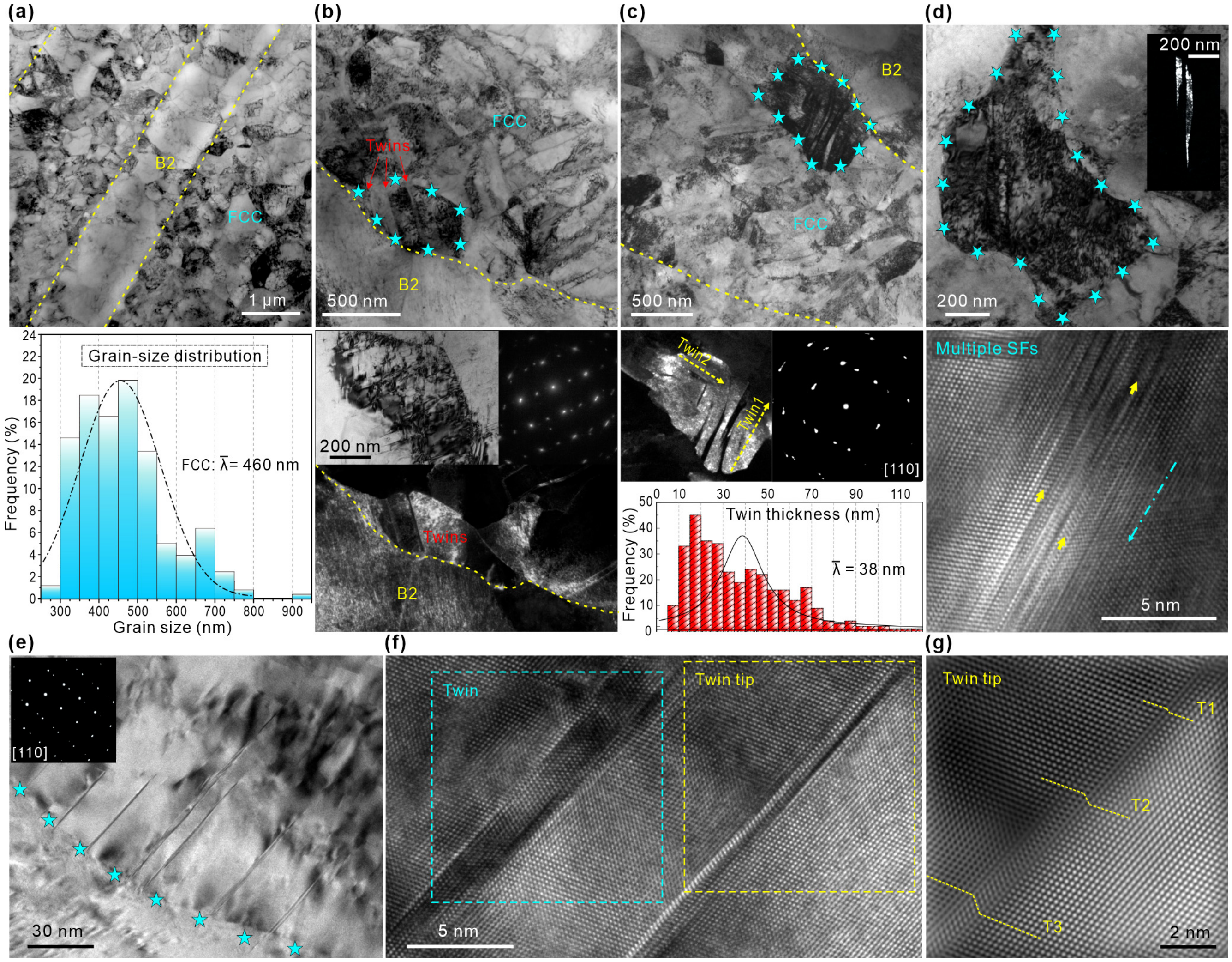

FIGURE 3

TEM images of deformation substructure. (a) Upper: FCC lamellae exhibiting denser dislocations than B2 lamellae. Under: FCC grain-size distribution. (b) Upper: twins formed near the B2 lamellar. High-density dislocations appear in B2 lamellae. Under: B2 phase and dense dislocations certified by SADP and dark-field (DF) image, respectively. Inset, dense dislocations in intergranular B2 precipitate. (c) Upper: extensive deformation twins. Under: DF image of a grain marked (upper) exhibiting two twinning systems (further evidenced by right SADP), and twin thickness distribution. (d) Upper: twinned grain with a severely-twisted morphology. Inset, DF image of twin tips. Under: multiple SFs forming the front end of twin tip, and microtwins marked by yellow arrows. Blue arrow indicates the twinning direction. (e) Deformation twins growing from grain boundary, and terminated inside the grain with twin tips. (f) High-resolution twin (blue dotted frame) and twin tip (yellow dotted frame) for (e). (g) Inverse fast Fourier transform (IFFT) of yellow-dotted-frame region in (f) showing an atomic-scale transition of twin tip from one-atomic-layer SF (T1) to three-atomic-layer twin (T3) when approaching the grain boundary. In (a–g) all grain and phase boundaries are marked by blue pentagons and yellow lines, respectively.

phase (hetero-)lamellae (Fig. 2a, b). What's different is the recrystallized grains in our UFG EHEA rather than simple phase bands in the as-cast EHEA (Fig. 2c). The FCC (face-centered-cubic) lamellae with average thickness of ~1.85 μm correspond to NiFeCo-rich grains (average size of ~460 nm), while the B2 (ordered body-centered-cubic) lamellae with ~1.32 μm are NiAl-rich grains (~540 nm) (Fig. 2d). Also, we noted the existence of ordered FCC ($L1_2$) nanoparticles in few FCC grains (Supplementary Fig. 4). (ii) By controlling thermo-mechanical treatments, we explored this EHEA's phase instability, which resulted in abundant Al-rich B2 precipitates distributed at grain boundaries in FCC lamellae [4,48,49] (Fig. 2c, d). During annealing, these intergranular B2 precipitates acted to pin grain boundaries to retard grain growth, which prevented the degradation of recrystallized lamellae [50,51]. In addition, the local variation in pinning efficiency enabled a multimodal size distribution of FCC grains (Fig. 3a). Therefore, we successfully prepared an ultrafine-grain decorated hierarchical hetero-lamellar structure, as illustrated by schematic diagrams in Fig. 2f and Supplementary Fig. 3.

Note that the above precipitation reaction changed the composition distribution in FCC lamellae. This change is characterized with Al depletion from the FCC lamellae owning to the formation of intergranular Al-rich B2 phase. Specifically, the average Al concentration decreased by 50% from the as-cast ~11 at% to the current ~5.5 at%, while the variation of other three elements is less than 15% (Fig. 2e, g). Unexpectedly, we found that this compositional modification due to the precipitation reaction of Al-rich B2 decreased the SFE of FCC grains in our

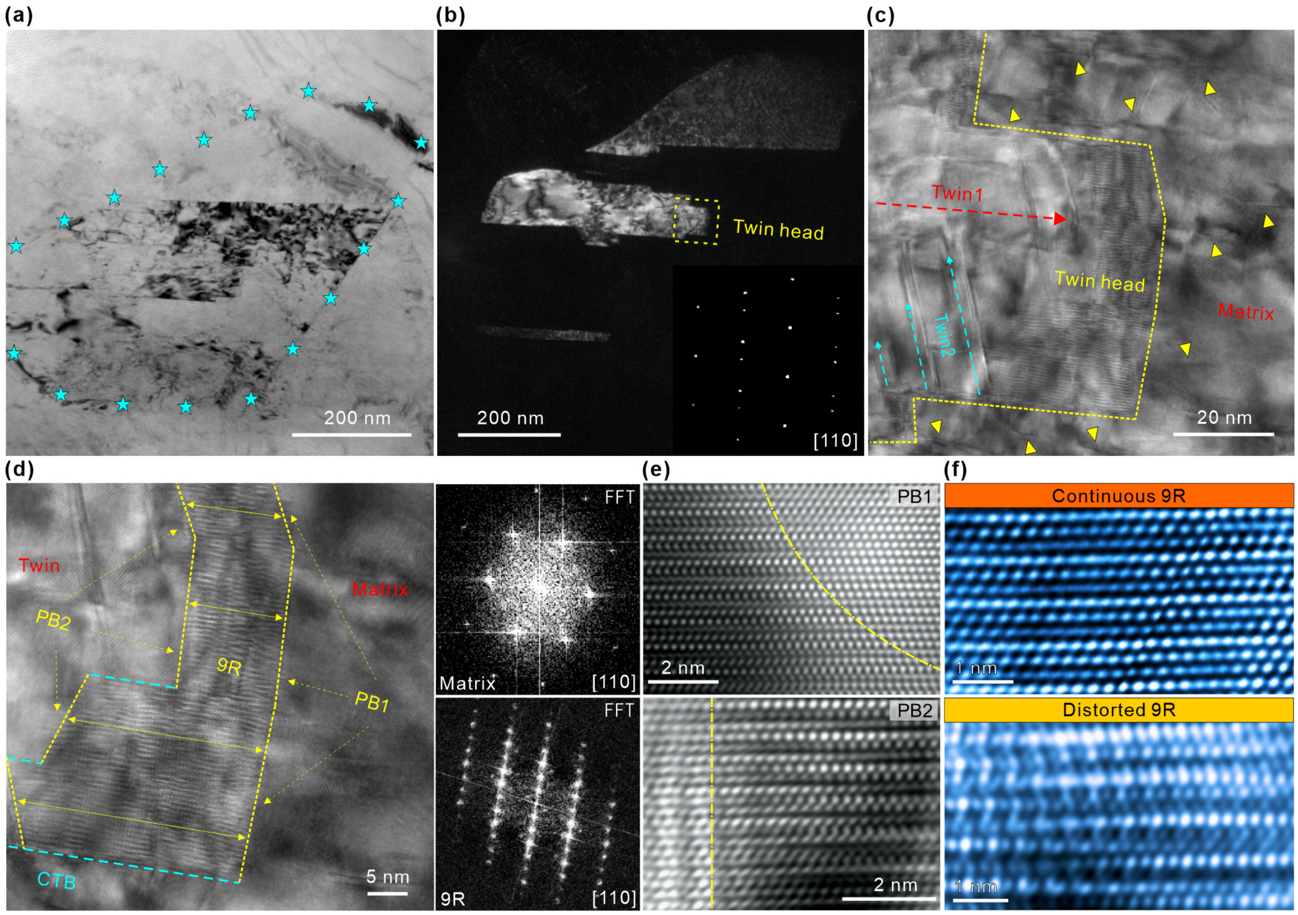

FIGURE 4

TEM images of the 9R-phase mediated DT. (a) Grain morphology. (b) DF grain morphology in (a). Inset, a twin SADP from this grain. (c) Enlarged yellow-dotted-frame region in (b) showing primary twin (twin1), secondary twins (twin2), and some dislocation and SF defects (marked by yellow triangles) in the front of twin head. (d) Further enlarged twin head in (c) showing two phase boundaries (PB1 and PB2), which bound a 9R phase evidenced by right FFT images. CTB, coherent twin boundary. (e, f) High-resolution images in (d) displaying a diffused PB1 and an abreast PB2 (e), and continuous and distorted 9R (f).

UFG EHEA. This is consistent with the trend observed in other Al-bearing FCC-type HEAs that the Al concentrations are closely related to SFEs, and the reduction of Al concentrations will lower the SFEs of materials, promoting extensive twinning deformation and even phase transformation [52–55]. In this study, similarly, we demonstrated the reduction of SFE in our UFG material by displaying some mutually supporting experimental evidences.

Furthermore, the present precipitation, as seen in traditional alloys, is a nucleation and growth process, associated with thermodynamic driving force and activation barrier for nucleation, and coupled with growth kinetics [48,56]. But this precipitation seems to occur much more readily in HEAs due to their multicomponent nature, which inevitably contains some binary systems with extremely-negative enthalpies (e.g., Ni-Al) [49,57]. Under proper thermomechanical conditions, hence, the second phase is easy to precipitate [49] (Supplementary Table 1). These features offer us an alternative material design approach—tailoring desirable structure, grain size, and intragranular chemical composition—at multiple scales. To our knowledge, this unique potential is generally inaccessible to traditional eutectic alloys. Therefore, we conclude that the compositionally-complex EHEAs can provide us with great opportunities to micro-engineer multiscale material characteristics for desirable SMSH behaviors.

Discussion

After completing the coordinated three-level design on structure, grain size, and intragranular composition, it naturally follows to analyze how this design leads to the multistage strain-hardening behavior observed in Fig. 1b. We uncovered the hardening mechanism responsible for each strain-hardening stage shown in Fig. 1b by detecting the dynamic evolution of deformation substructure, as elaborated below.

Upon tensile loading, soft lamellae of FCC-matrix grains started plastic deformation first in our UFG EHEA [4,58]. However, the soft FCC-matrix lamellae could not deform freely, due to the deformation constraint caused by still elastic B2 lamellae and the precipitate phase [4]. In this elastic–plastic deformation stage, geometrically necessary dislocations (GNDs) were blocked and piled up at lamellar/phase (hetero-)interfaces, consequently generating a long-range back stress in soft FCC grains [58–60]. The back stress is directional, and can offset some applied shear

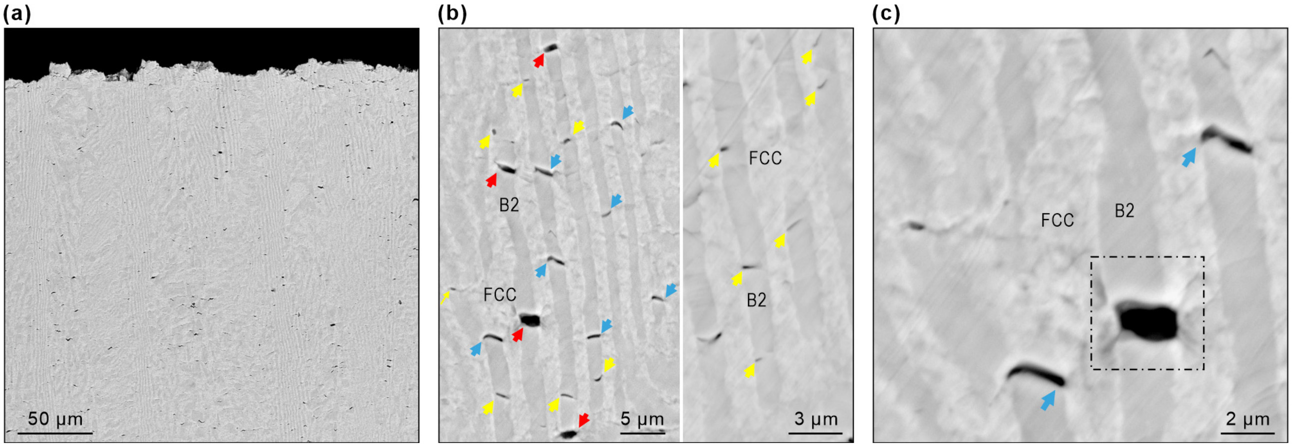

FIGURE 5

Typical SEM images of damage-evolution mechanisms. (a) The fractured end showing extensive uniformly distributed microcracks, instead of large (secondary) cracks usually seen in most cases. (b) Microcracks nucleated predominantly in B2 lamellae near phase interfaces, due to the stress concentration. Some microcracks terminate in B2 lamellae (left and right images, marked by yellow arrows), some run across whole B2 lamellae (left image, marked by blue arrows), and a few exhibit larger crack dimensions (left image, marked by red arrows). (c) Enlarged image indicating the crack propagation confined by adjacent ductile FCC lamellae, which is experimentally supported that (i) these observed microcracks show blunted crack-tips (blue arrows) near phase interfaces, and (ii) these microcracks running through B2 lamellae (black dotted frame) cannot penetrate FCC lamellae, and instead, they grow slowly along the direction of B2 lamellae with the assistance of ductile FCC lamellae.

stresses [60]. Therefore, this leads to higher apparent strength for FCC-matrix grains to significantly raise the global yield strength of our UFG EHEA.

The GND piling-ups against FCC/B2 hetero-interfaces also exerted forward stress in the hard B2 grains [60], which promoted their plastic deformation. When FCC and B2 grains co-deformed plastically, the soft FCC grains obviously underwent higher plastic strain (Fig. 3a), resulting in a heterogeneous deformation [58–60]. There has to be strain gradient near hetero-interfaces to accommodate the heterogeneous deformation. The strain gradient needs to be sustained by GNDs, thereby producing the back stress in the soft FCC grains and the forward stress in the hard B2 grains, which collectively produce a hetero-deformation induced hardening [60] at true strains of ~3–8% (Seg. II in Fig. 1b).

At true strain of ~7%, deformation twins were detected in several large FCC grains (>0.55 μm) at certain locations near the hard B2 precipitates/lamellae (Fig. 3b). This is because these locations readily trigger high local back stress due to the GND pile-ups, thus activating twins to alleviate local stress concentrations [6,61]. Concurrently, the reduced SFE promotes the dissociation of perfect dislocations for twinning [15,17]. When the true strain increased to ~11%, extensive twins were observed with average thickness of ~38 nm, and even secondary deformation twins appeared in some FCC grains (Fig. 3c). Both dynamic twin–dislocation and twin–twin interactions can lead to extraordinary strain-hardening behavior, as observed in these reported low-SFE HEAs with twinning deformation [18–20]. Consequently, our UFG EHEA exhibits an increased strain-hardening rate at true strains of ~8–11.5% (Seg. III in Fig. 1b).

Characterization of the atomic-scale structure of twin tips revealed a twinning route [62,63] (Fig. 3d and Supplementary Fig. 6) that is different from the classical pole mechanism [16]. Multiple Shockley partial dislocations with Burgers vector $[\overline{1}\overline{1}2]/6$ were emitted on (1 1 1) glide planes successively from the same grain boundary, leaving behind multiple stacking faults (SFs). These multiple SFs are on alternative slip planes, transforming the FCC-matrix structure into a hexagonal-close-packed (HCP) structure. With the propagation of these partial dislocations, some partials were emitted between the SFs, transforming the HCP structure into twins of varying thicknesses. Here, these observed multiple SF-decorated twin boundaries are unique to this twinning mechanism, which should cause additional multiple SF-mediated hardening. It is the first time that this twinning mechanism is detected in UFG materials, although it has been revealed by simulations and experiments in nanocrystalline materials [62,63]. But essentially, both of them are an energy reduction-related process, which drives the transformation of high-energy SFs into low-energy twins [62].

Furthermore, high dislocation density was observed in hard B2 precipitates and lamellae (Fig. 3b), which should also have contributed to strain hardening at true strains of ~8–11.5%. Such profuse dislocation activities were promoted by the forward stress in hard B2 precipitates/lamellae, which was reported to be many times higher near these hetero-interfaces than the applied stress [4,60], and could help B2 components with plastic deformation. Consequently, the deformation evolved dynamically from the intergranular hetero-deformation to dual-phase co-deformation. However, this co-deformation will gradually lower the deformation constraint, and weaken the hetero-deformation induced hardening [60]. Therefore, the strain-hardening rate decreased gradually at true strains of ~12–15.5% (Seg. IV in Fig. 1b).

With further deformation (~16–18.5%), surprisingly, the strain-hardening rate became almost constant (Fig. 1b). Extensive microstructural examinations revealed that two other types of DT activities (Figs. 3e–g and 4) preferentially occurred in the remaining small grains (~0.3–0.5 μm). This implies that grain size may have played a significant role in activating the three types of DT. In other words, this may indicate a strong grain-

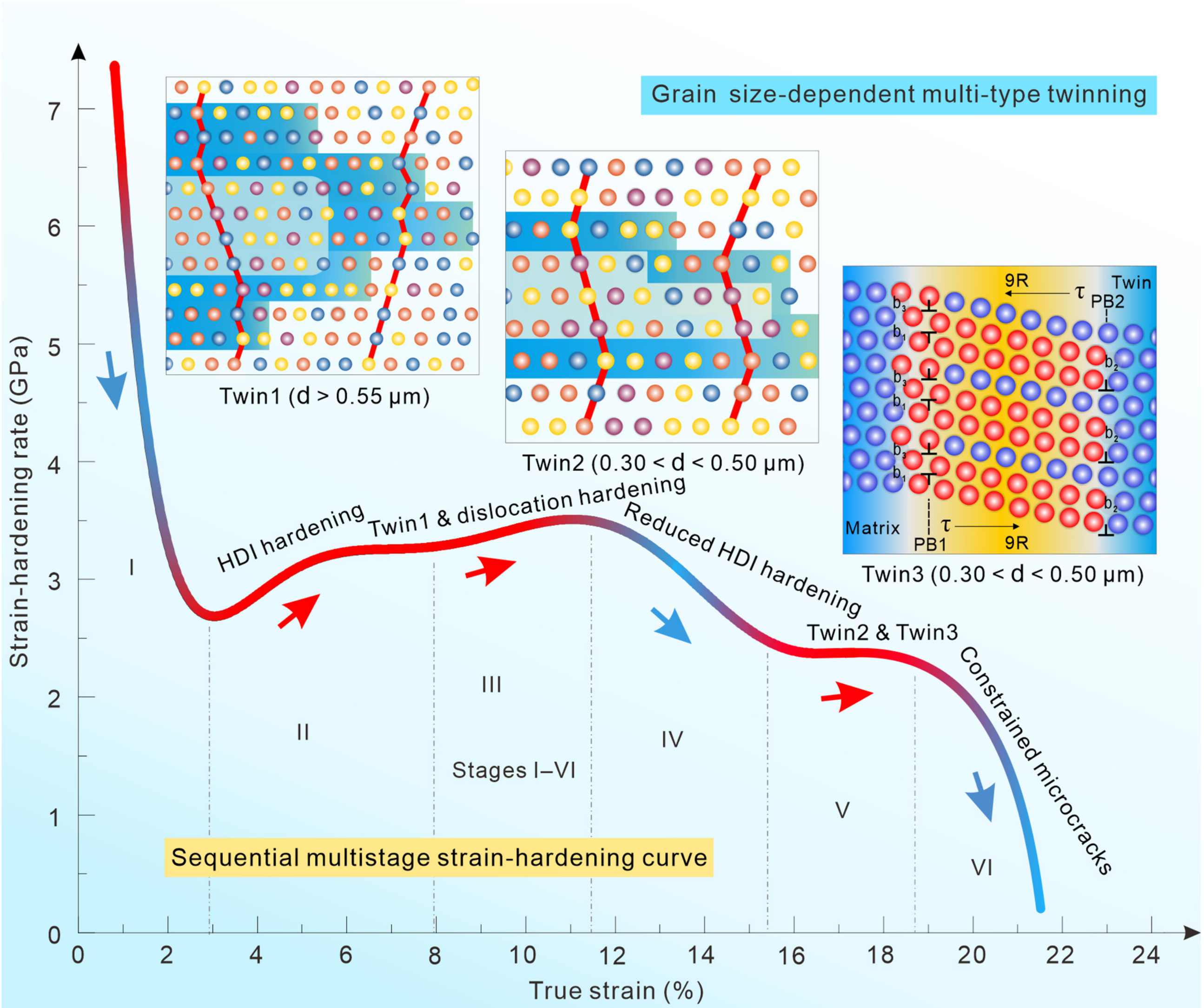

FIGURE 6

Schematic illustration of sequential multistage strain hardening assisted by grain size-dependent multi-type twinning in our UFG EHEA. The twin1-type twinning mode is primarily detected in large grain size (d > 0.55 μm), while the twin2- and twin3-type twinning activities preferentially occur in the remaining small grains, and particularly in these grains of 0.3 < d < 0.5 μm.

size dependence of DT types [16,17,21]. Coupled with the simultaneous formation of other defects including SFs, SF ribbons, Lomer-Cottrell locks, etc. (Supplementary Figs. 7, 8), the DT-dominated multiple mechanisms acted synergistically to promote the improved strain-hardening rate [20,64,65] (Seg. V in Fig. 1b). Therefore, in the next section, we will continue to discuss the corresponding twinning mechanisms so as to analyze their specific contributions to the remarkable multistage hardening behavior tailored in our UFG EHEA.

Fig. 3e–g shows one of the two types of DT, analogous to that of Supplementary Fig. 6, formed through Shockley partial dislocation emission from grain boundaries [66]. Differently, these partials glide on parallel and adjacent {1 1 1} planes. Moreover, high-resolution image (Fig. 3f, g) of twin tip clearly exhibits a twin-thickness evolution from one-atomic-layer SF to three-atomic-layer twin. This thickness variation, also seen as the twin growth, derives from successive partial emission from grain boundaries [17]. This twinning mechanism has been detected primarily in nanograins [16,66]. The present twinning in ultrafine grains (Fig. 3e) may be attributed to the decreased SFE in our UFG EHEA. For example, Wang et al. observed similar trends in CuZn alloys [17] that low SFE promoted the partial emission from grain boundaries in ultrafine grains of a few hundred nanometers, thereby facilitating twinning deformation. It is observed here that the dislocation density in twinned grains is ~4–8 × 10^{14} m^{-2}, which is many times higher than in grains without twins (~1 × 10^{14} m^{-2}). This indicates that this DT scenario can significantly increase strain hardening.

Another twinning mechanism (detected in Fig. 4a and b) was formed through the migration of 9R-phase mediated Σ3{1 1 2} incoherent twin boundaries (ITBs) [67–71]. These Σ3{1 1 2} ITBs comprise a periodic array of three different partial dislocations, $\mathbf{b_1}$, $\mathbf{b_2}$, and $\mathbf{b_3}$ ($\mathbf{b_1} + \mathbf{b_2} + \mathbf{b_3} = 0$). Upon tensile loading, two partials $\mathbf{b_1}$ and $\mathbf{b_3}$ glide forward on (1 1 1) planes under the applied shear stress, while the $\mathbf{b_2}$ partial is left behind because the applied stress is oriented to drive the $\mathbf{b_2}$ partial backward. This also creates two SFs for every three partials, which increase the system energy. When the local stress dynamically fluctuates to weaken the backward driving force for the $\mathbf{b_2}$ partial, it will glide forward toward $\mathbf{b_1}$ and $\mathbf{b_3}$ to reduce SFE [70]. A 9R phase bounded by two phase boundaries was formed between the twin and the matrix (Fig. 4c–e). This process could repeat itself, causing the migration of ITBs (i.e., the 9R phase) to the matrix direction to grow the twin (Fig. 4d). In general, the 9R phase and its mediated DT are rarely detected in medium-to-high SFE materials. For example, even under high shear stresses the 9R phase has not been observed in Al or its alloys, in sharp contrast to the low-SFE Cu, wherein the 9R can form and propagate under shear stresses [68,69]. Recently, Xue et al. [67] discovered a deformation-induced 9R phase with tens of nm in width in UFG Al by using a laser-induced projectile impact testing technique which enabled ultrahigh strain rates of $\sim 10^7$–10^8 s^{-1} during plastic deformation. To accommodate the deformation under such high strain rates, the formation of 9R phase via dissociations of ITBs could occur even if there is a high-energy barrier caused by the high SFE of Al.

Therefore, we believe that in our UFG EHEA these giant 9R configurations (maximum width of $\sim$50 nm, Supplementary Fig. 9) formed during tensile deformation (strain rate of $\sim 2.5 \times 10^{-4}$ s^{-1}) are due to (i) the reduced SFE promoting the dissociation of ITBs by the emission of three partial dislocations for 9R-phase nucleation, and (ii) the hierarchical heterostructure triggering high local stress for 9R-phase migration and growth. Prior 2D and 3D molecular dynamics simulations [71] revealed that pronounced interactions of dislocations with 9R phase can contribute to substantial strain hardening during deformation. In our UFG EHEA, the 9R may experience more complex interactions, and we noticed extensive defect barriers, such as lattice dislocations, SFs, and microtwins, in the front of the 9R (Fig. 4c and Supplementary Fig. 7). Furthermore, prominent partial dominated migration scenarios were observed at locations where the 9R was distorted (Fig. 4f) due to their interactions with defects during deformation. This evolution of the continuous 9R to the distorted one indicates that the 9R also makes significant contribution to strain hardening [67,71]. Hence, the 9R phase and the twinning mediated by it should certainly have contributed to strain hardening (Seg. VI in Fig. 1b).

These multiple strain hardening mechanisms described above are sequentially activated, leading to the observed remarkable SMSH behavior. To the best of our knowledge, this is the first time that multi-type twinning is observed in HEAs/EHEAs, let alone with ultrafine grains, which sequentially occurs to assist the SMSH. Moreover, these corresponding twinning mechanisms are all different from the classical pole mechanism operating in large micro-sized grains, in which one partial dislocation forms a whole twin via climbing a screw dislocation pole to adjacent slip planes [16]. We indicated that in our UFG EHEA, the compositional modification about the great reduction of Al content resulted in low SFE of FCC grains and thus extensive deformation twins, which are markedly different from our recent work focusing primarily on heterostructural design [4]. Indeed, when controlling the precipitation reaction of Al-rich B2 phase so that the Al content in FCC grains was not reduced too much, deformation twinning would be significantly inhibited (Supplementary Text 1). In addition, we also observed this phenomenon in other EHEA systems by controlling the precipitation reaction to reduce SFEs and thus induce deformation twins, irrespective of the twinning type and density. Therefore, it is necessary to focus on establishing the relationship between the precipitation reaction and specific SFE value in the future research to tailor desired low SFEs, thus achieving pronounced twinning deformation to reinforce the SMSH behavior for unprecedented performance improvement.

Finally, we analyzed the damage-evolution mechanism (Fig. 5a). Different from our recently-reported work [4], in our SMSH EHEA we detected the initial microcrack nucleation in B2 lamellae rather than in FCC lamellae (Fig. 5b), despite of the higher deformability of B2 lamellae than intergranular B2 precipitates. This change can be attributed to the improved deformability of FCC lamellae encouraged by the multi-type DT activities. Furthermore, we found that these multi-type DT-reinforced FCC lamellae could effectively arrest microcracks in adjacent B2 lamellae to inhibit their propagation/coalescence during deformation (Fig. 5c). This can delay the onset of crack-related global damage, allowing the residual inter-/intra-granular strain-hardening abilities to last longer. Correspondingly, the strain-hardening curve in its final stage shows a slow downward trend, in sharp contrast to the quick dropping in the as-cast EHEA (Fig. 1b).

Conclusion

Our tailored SMSH behavior effectively led to exceptional ductility in high-strength UFG EHEAs, accompanied with high strength difference. The SMSH behavior was enabled by the coordinated three-level design so that an earlier hardening mechanism increased the flow stress to activate the following hardening mechanism. Upon straining the structural heterogeneity first came into play, producing a hetero-deformation induced (HDI) intergranular hardening. This heterogeneity simultaneously offered high back stress in FCC grains and forward stress in B2 grains. Consequently, a composite intragranular hardening was triggered in which FCC grains began the first type of DT, while B2 grains underwent profuse dislocation activities. The first type of DT (Twin1) was found associated with the formation of multiple SFs, which produced additional hardening to further elevate the flow stress. This subsequently activated two other types of DTs (Twin2 & Twin3) in the remaining relatively-small FCC grains, leading to further intragranular hardening. Finally, these multi-type DT-reinforced FCC grains could delay the crack-related global damage, prolonging the residual inter-/intra-granular strain hardening to large plastic strains.

The corresponding SMSH process was explained with schematic illustrations, see Figs. 2f and 6. In addition, we performed some other supporting experiments to further confirm the extraordinary hardening effect from our tailored SMSH behavior (see Supplementary Texts 2 and 3). Overall, this work sheds light on a peculiar SMSH behavior assisted by multi-type twinning in UFG EHEAs, which provides a promising strategy for improving uniform elongation and ultimate-yield strength difference of high-strength UFG materials. Note that the UFG EHEA investigated in this work is not yet specifically optimized for the best possible SMSH behavior. With improved intergranular precipitation reaction for as low SFEs as possible, we expect further optimization of SMSH, and thus more considerable property improvement. The present SMSH strategy might be applicable to other EHEA systems and some dual-phase metallic materials, such as austenite–martensite duplex steels. Furthermore, we anticipate this strategy to be extremely promising in intrinsic low-SFE metallic materials [72], especially in EHEAs.

Materials and methods

Specimen preparation

Alloy ingots with a nominal composition of $Fe_{20}Co_{20}Ni_{41}Al_{19}$ (at %) were prepared using arc-melting elemental ingredients with a purity > 99.95 wt% in a Ti-gettered high-purity argon atmosphere. The ingots were re-melted at least five times and then drop-cast into a 40 mm × 110 mm × 10 mm copper mould. Small pieces [dimensions: 100 mm (length) × 35 mm (width) × 4.2 mm (thickness)] were extracted from ingots, and subjected to multi-pass cold-rolling to ~83% reduction in thickness using a laboratory-scale two-high rolling machine. The cold-rolled sheets were non-isothermally annealed to various temperatures. More specifically, three cold-rolled samples were annealed from room temperature to 660, 740, and 780 °C, respectively, with a constant heating rate of 10 °C min^{-1}, held at these three temperatures for 1 h and then water quenched immediately. We denote them as the SMSH EHEA, the inferior SMSH EHEA-1, and the inferior SMSH EHEA-2, respectively. Of the three samples, the SMSH EHEA (annealed at 660 °C) exhibits an optimal SMSH behavior (assisted by deformation twins), as shown in the main text. The inferior SMSH EHEA-1 (annealed at 740 °C) and the inferior SMSH EHEA-2 (780 °C) were used as reference materials to illustrate the important role of SMSH (see Supplementary Text 1, and Supplementary Figs. 10 and 11 for more details).

SEM and TEM

Electron back-scattering diffraction (EBSD) and scanning-electron-microscope (SEM) observations were conducted in a CamScan Apollo 300 SEM equipped with a HKL–Technology EBSD system. TEM and HAADF-STEM analyses were conducted on a JEM–2100 F at 200 kV. EBSD specimens were initially polished with the 2000-grit SiC paper and subsequently electrochemically polished using a 6% perchloric acid + 30% *n*-butyl alcohol + 64% methyl alcohol solution (vol.%) at a direct voltage of 30 V at room temperature. TEM specimens were first mechanically ground to ~30-μm thickness and then twin-jet electropolished using a mixture of the 90% ethanol and 10% perchloric acid (vol.%).

Tensile and loading–unloading–reloading (LUR) tests

Dogbone-shaped tensile samples with a cross section of $3.2 \times 0.7\ mm^2$ and a gauge length of 13 mm were cut from cold-rolled sheets using electrical discharging. Room-temperature tensile and LUR tests were conducted in an MTS Criterion Model 44 machine with an initial strain rate of $2.5 \times 10^{-4}\ s^{-1}$. The direction of tensile tests was parallel to the rolling direction. To obtain reproducible tensile date, all tensile tests were repeated five times at least. All tensile tests were conducted, using a 10-mm extensometer to monitor the strain. The condition for LUR tests was the same as that of the monotonic tensile test. Upon straining to a designated strain at the strain rate of $2.5 \times 10^{-4}\ s^{-1}$, the specimen was unloaded in load mode to 20 N at the unloading rate of 200 N min^{-1}, followed by reloading at a strain rate of $2.5 \times 10^{-4}\ s^{-1}$ to the same applied stress before the next unloading.

The processing method of strain hardening curve

(i) Based upon the engineering strain (ε_E) and engineering stress (σ_E), the true strain (ε_T) and true stress (σ_T) were calculated from the yield to the ultimate tensile strength:

$$\sigma_T = \sigma_E \times (1 + \varepsilon_E) \quad (1)$$

$$\varepsilon_T = \ln(1 + \varepsilon_E \quad (2)$$

(ii) The strain-hardening rate (θ) were calculated:

$$\theta = d\sigma_T/d\varepsilon_T \quad (3)$$

As shown in Supplementary Fig. 14a, the resultant curve of strain-hardening rate versus true strain features a remarkable multistage strain-hardening behavior (i.e., stages I–VI), yet accompanied by obvious short-range noises.

(iii) To better exhibit the strain-hardening behavior, in this work the experimental curve was smoothed by fitting a high order polynomial (using OriginPro software) to remove the irregularities and fluctuations. The fitting principle is that the linear law/rule of the curve obtained in step (ii) must not be changed, as displayed in Supplementary Fig. 14b. More specifically, the undulations of the strain-hardening rate is not the result of the polynomial fit, but the true functional dependence of stress on strain.

Declaration of Competing Interest

The authors declare that they have no known competing financial interests or personal relationships that could have appeared to influence the work reported in this paper.

Acknowledgements

We thank J. Wang at University of Nebraska-Lincoln for his insightful and constructive comments on twinning mechanisms. We thank T. Yang at City University of Hong Kong, Z.B. Jiao at Hong Kong Polytechnic University, and J.P. Liu at Chinese Academy of Sciences for their help with tensile tests at the cryogenic temperature. We also thank N. Min at Shanghai University for her help with TEM/STEM characterization. Y.B.Z. is grateful for financial support from the National Key Research and Development Program of China (2018YFF0109404), the National Natural Science Foundation of China (U1732276, U1860202), and the National Key Research and Development Program of China (2016YFB0300401, 2016YFB0301401). Y.T.Z. is grateful for financial support from the National Natural Science Foundation of China (Grant No. 51931003). T.X.Z. is grateful for financial support from the National Natural Science Foundation of China (Grant No. 51704193). Z.S. is grateful for financial support from the National Natural Science Foundation of China (Grant No. 51904184).

Author contributions

Y.B.Z., Y.T.Z., and P.J.S. designed the study. P.J.S. carried out the main experiments. Y.L., B.Y., Z.S., and T.X.Z. processed the alloy samples. Y.T.Z., P.K.L., Y.Z., W.L.R., Y.B.Z., and P.J.S. analyzed the data and wrote the main draft of the paper. J.C.P. and P.F. H. conducted the TEM characterization. All authors discussed the results and commented on the manuscript.

Competing financial interest statement

The authors declare no competing financial interests.

Appendix A. Supplementary data

Supplementary data to this article can be found online at https://doi.org/10.1016/j.mattod.2020.09.029.

References

[1] D. Raabe, C.C. Tasan, E.A. Olivetti, Nature 575 (2019) 64–74.
[2] L.F. Liu et al., Mater. Today 21 (2018) 354–1352.
[3] Y.T. Zhu, X.Z. Liao, Nat. Mater. 3 (2004) 351–352.
[4] P.J. Shi et al., Nat. Commun. 10 (2019) 489.
[5] Y.M. Wang et al., Nature Mater. 17 (2018) 63–71.
[6] Y.M. Wang et al., Nature 419 (2002) 912–915.
[7] R.O. Ritchie, Nat. Mater. 10 (2011) 817–822.
[8] Z. Cheng et al., Science 362 (2018) 559.
[9] Z.F. Lei et al., Nature 536 (2018) 546–550.
[10] Z.M. Li et al., Nature 534 (2016) 227–230.
[11] B. Gludovatz et al., Science 345 (2014) 1153–1158.
[12] E. Ma, X.L. Wu, Nat. Commun. 10 (2019) 5623.
[13] T. Yang et al., Science 362 (2018) 933–937.
[14] Y.J. Liang et al., Nat. Commun. 9 (2018) 4063.
[15] M.X. Yang et al., Proc. Natl Acad. Sci. USA 115 (2018) 7224–7229.
[16] Y.T. Zhu, X.Z. Liao, X.L. Wu, Prog. Mater. Sci. 57 (2012) 1–62.
[17] Z.W. Wang et al., Scripta Mater. 60 (2009) 52–55.
[18] Q.Q. Ding et al., Nature 574 (2019) 223–227.
[19] Q.Q. Ding et al., Mater. Today 25 (2019) 21–27.
[20] Z.J. Zhang et al., Nat. Commun. 6 (2015) 10143.
[21] Q. Yu et al., Nature 463 (2010) 335–338.
[22] M.W. Cheng et al., Science 300 (2003) 1275–1277.
[23] Z.M. Li et al., Acta Mater. 164 (2019) 400–412.
[24] H. Shahmir et al., Mater. Sci. Eng. A 676 (2016) 294–303.
[25] G.S. Sun et al., Mater. Charact. 110 (2015) 228–235.
[26] J.S. Li et al., J. Mater. Sci. 53 (2018) 10442–10456.
[27] B. Cantor et al., Mater. Sci. Eng. A 375 (377) (2004) 213–218.
[28] J.W. Yeh et al., Adv. Eng. Mater. 6 (2004) 299–303.
[29] Y. Zhang et al., Prog. Mater. Sci. 61 (2014) 1–93.
[30] Y.P. Lu et al., Sci. Rep. 4 (2014) 6200.
[31] S. Guo, C. Ng, C.T. Liu, Mater. Res. Lett. 1 (2013) 228–232.
[32] Y.H. Zhao et al., Adv. Mater. 18 (2006) 2949–12593.
[33] B.B. He, M.X. Huang, Mater. Res. Lett. 6 (2018) 365–371.
[34] C.S. Lei et al., Scripta Mater. 162 (2019) 421–425.
[35] G. Liu et al., Nat. Mater. 12 (2013) 344–350.
[36] X. Jin et al., Mater. Lett. 216 (2018) 144–146.
[37] X. Jin et al., Materialia 10 (2020) 100639.
[38] I.S. Wani et al., Mater. Res. Lett. 4 (2016) 174–179.
[39] T.H. Wang et al., J. Alloy. Compd. 766 (2018) 312–317.
[40] I.S. Wani et al., Mater. Sci. Eng. A 675 (2016) 99–109.
[41] S.R. Reddya et al., Intermetallics 114 (2019) 106601.
[42] K. Edalati et al., Mater. Res. Lett. 3 (2015) 197–202.
[43] Y.H. Zhao et al., Scripta Mater. 59 (2008) 627–630.
[44] Y.H. Zhao et al., Mater. Sci. Eng. A 525 (2009) 68–77.
[45] S.R. Reddy et al., Sci. Rep. 9 (2019) 1396.
[46] S.R. Reddy et al., Mater. Sci. Eng. A 764 (2019) 138226.
[47] I. Gutierrez-Urrutia, D. Raabe, Acta Mater. 60 (2012) 5791–5802.
[48] B. Schuh et al., Acta Mater. 96 (2015) 258–268.
[49] F.L. Meng, J.W. Qiu, I. Baker, J. Mater. Sci. 49 (2014) 1973–1983.
[50] M. Schinhammer et al., Acta Mater. 60 (2012) 2746–2757.
[51] W. Yang, D.S. Yan, L.J. Rong, Scripta Mater. 68 (2013) 587–590.
[52] T.S. Cao et al., Mater. Lett. 164 (2016) 344–347.
[53] C.X. Wang et al., Appl. Phys. Lett. 114 (2019).
[54] X. Sun et al., Nanomaterials 10 (2020) 59.
[55] Q.K. Zhao et al., Physica B 566 (2019) 30–37.
[56] B. Gwalani et al., Acta Mater. 153 (2018) 169–185.
[57] S. Singh et al., Acta Mater. 59 (2011) 182–190.
[58] C.X. Huang et al., Mater. Today 21 (2018) 713–719.
[59] E. Ma, T. Zhu, Mater. Today 20 (2017) 323–331.
[60] Y.T. Zhu, X.L. Wu, Mater. Res. Lett. 7 (2019) 393–398.
[61] D. Choudhuri et al., Acta Mater. 165 (2019) 420–430.
[62] J. Wang, H.C. Huang, Appl. Phys. Lett. 85 (2004) 5983.
[63] L.H. Wang et al., Nat. Commun. 8 (2017) 2142.
[64] C.E. Slone et al., Acta Mater. 165 (2019) 496–507.
[65] Y. Ma et al., Acta Mater. 148 (2018) 407–418.
[66] X.Z. Liao et al., Appl. Phys. Lett. 83 (2003) 632–634.
[67] S.C. Xue et al., Nat. Commun. 8 (2017) 1653.
[68] J. Wang, A. Misra, J.P. Hirth, Phys. Rev. B 83 (2011) 064106.
[69] J. Wang, N. Li, A. Misra, Philos. Mag. 93 (2013) 315–327.
[70] J. Wang et al., Appl. Phys. Lett. 95 (2009) 021908.
[71] Q. Li et al., Adv. Mater. 30 (2018) 1704629.
[72] Y.Z. Tian et al., Mater. Charact. 126 (2017) 74–80.